Supporting Information

for

Boron-doped Diamond Electrode Outperforms the State-of-the-art Electrochemiluminescence from Microbeads Immunoassay

Kohei Sakanoue,[‡] Andrea Fiorani,*[‡] Claudio Ignazio Santo,[†] Irkham,[‡,#] Giovanni Valenti,[†] Francesco Paolucci[†] and Yasuaki Einaga*[‡]

[‡]*Department of Chemistry, Keio University, 3−14−1 Hiyoshi, Yokohama 223−8522, Japan*

[†]*Department of Chemistry "G. Ciamician", University of Bologna, Via Selmi 2, 40126, Bologna, Italy*

[#]*Present address: Department of Chemistry, Padjadjaran University, Jalan Raya Bandung Sumedang Km. 21, Sumedang 45363, Indonesia*

email: andrea.fiorani@keio.jp

email: einaga@chem.keio.ac.jp

Table of Contents

1. Raman spectroscopy, SEM and GD-OES of the BDD electrode

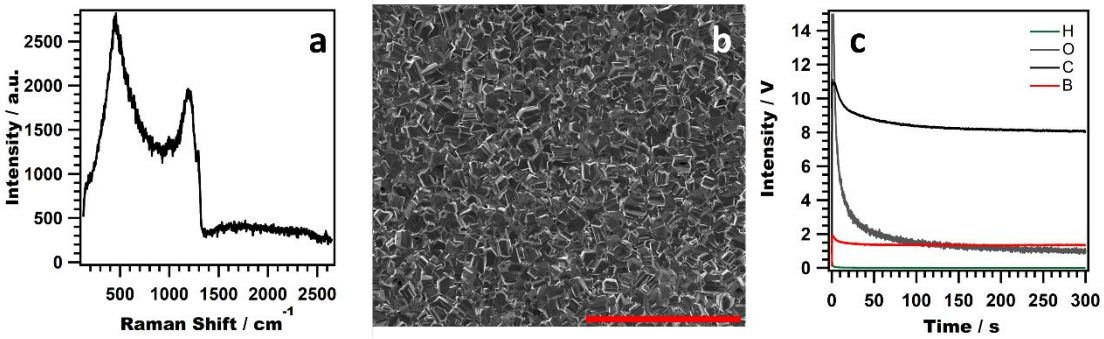

Figure S1. Raman spectrum (a), SEM image (scale bar: 30 μm) (b) and GD-OES profile (c) of BDD electrode.

Raman spectrum of BDD shows two bands at around 450 $cm^{-1}$and 1200 cm^{-1}, which are attributed to the B-B and B-C vibrations, respectively, typically observed in highly boron-doped diamond. The absence of a peak around 1530 cm^{-1} (G band) indicates the absence of sp^2 carbon. The peak at 1300 cm^{-1} results from the interaction of the diamond discrete zone-center optical phonon and a continuum of electronic excitations.[1]

The BDD is polycrystalline with an average grain size around 3μm, where mainly polygonal crystals were observed, characteristic of (111) facet compared to triangular (100) facet.

From Glow Discharge Optical Emission Spectrometry (GD-OES), the boron concentration was calculated as 2.06% (Figure S1c) by comparing the B/C ratio with that of a BDD electrode whose concentration had been directly measured by Secondary-ion mass spectrometry (SIMS) as 1.92%.[2] Further details on BDD electrodes are available in our previous characterization study.[2]

2. Cyclic voltammetry of BDD and Pt electrodes

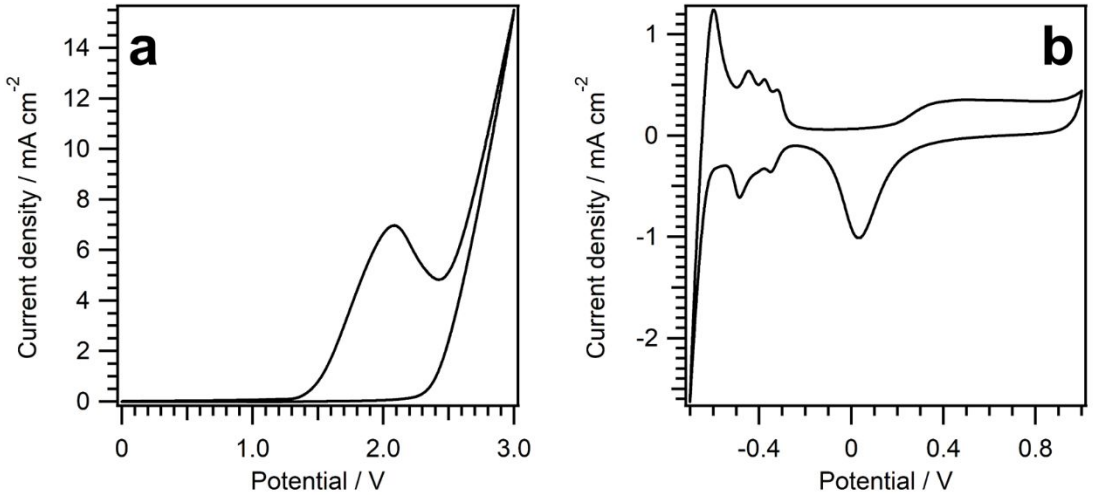

Figure S2. CV of 1% BDD (a) and Pt (b) electrodes in 0.2 M PB (pH 7.0). Scan rate is 300 mV s^{-1}.

3. Beads loading with ruthenium complex-immunoglobulin conjugate

3.1 Synthesis of ruthenium complex-immunoglobulin-biotin conjugate (Ru-IgG-biotin)

Immunoglobulin G (**IgG**, 5.7 mg ml^{-1}) was diluted to 0.2 mg ml^{-1} with 0.1 M potassium phosphate, pH 8.4. Biotinamidohexanoic acid N-hydroxysuccinimide ester (**biotin**) was dissolved in anhydrous dimethyl-sulfoxide (DMSO) at a concentration of 0.132 mM and 50 µL added to 1 ml of **IgG** solution (in proportion of five times in moles, **biotin**/**IgG**). After 90 minutes of incubation at 25 °C with a rotating mixer, the solution was dialyzed at 4 °C overnight against 0.15 M potassium phosphate/0.15 M NaCl (pH 7.8) to obtain **IgG-biotin** (Scheme S1).

Scheme S1. The biotinylation of immunoglobulin G (IgG).

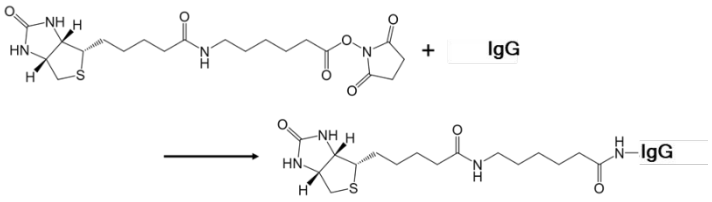

Ruthenium labelling of **IgG-biotin** was conducted as shown in Scheme S2 and S3. N, N'-dicyclohexylcarbodiimide (DCC, 8.2 µmol) and N-hydroxysuccinimide (NHS, 18.0 µmol) were dissolved in 300 µL dried chilled dimethyl N, N-formamide (DMF) with stirring. To this solution, it was added 1.62 µmol of bis(2,2'-bipyridine)-[4-(4'-methyl-2,2'-bipyridin-4-yl)butanoic acid] ruthenium bis(hexafluorophosphate) dissolved in 100 µL chilled DMF. The mixture was stirred on ice for 30 min, before returning to room temperature (25 ℃) and stirring was continued for another 4.5 h. The reaction mixture was then chilled (-18 ℃), and the solids were removed by centrifugation (Scheme S2). The obtained ruthenium complex solution was added to the dialysed **IgG-biotin** solution (Scheme 3) at a ratio of 50 µL to 1 mL, and the mixture was incubated with a rotating mixer for 90 min at 25 ℃. The **Ru-IgG-biotin** conjugate was dialyzed overnight against 25 mM potassium phosphate/0.15 M NaCl (pH 7.0).

Scheme S2. The ruthenium activation with N-hydroxysuccinimide.

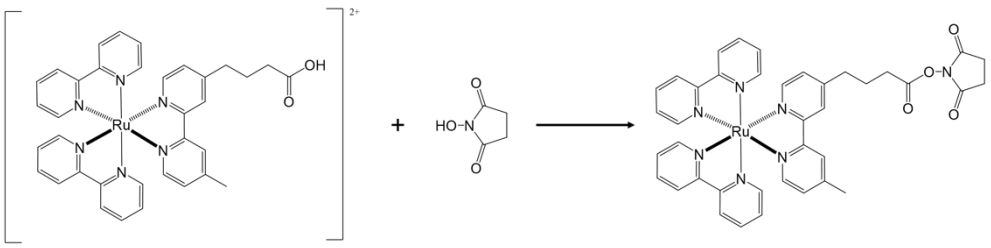

Scheme S3. The ruthenium labelling of **IgG-biotin**.

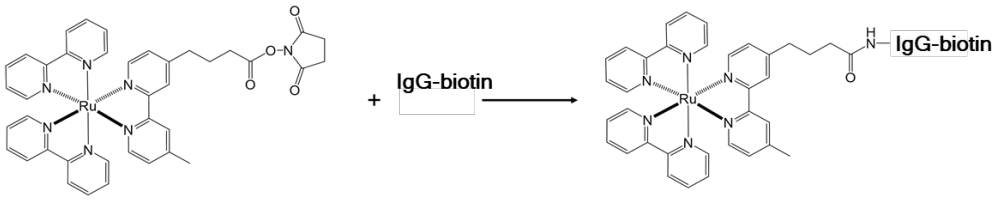

3.2 Adsorption and emission spectra of the ruthenium conjugate

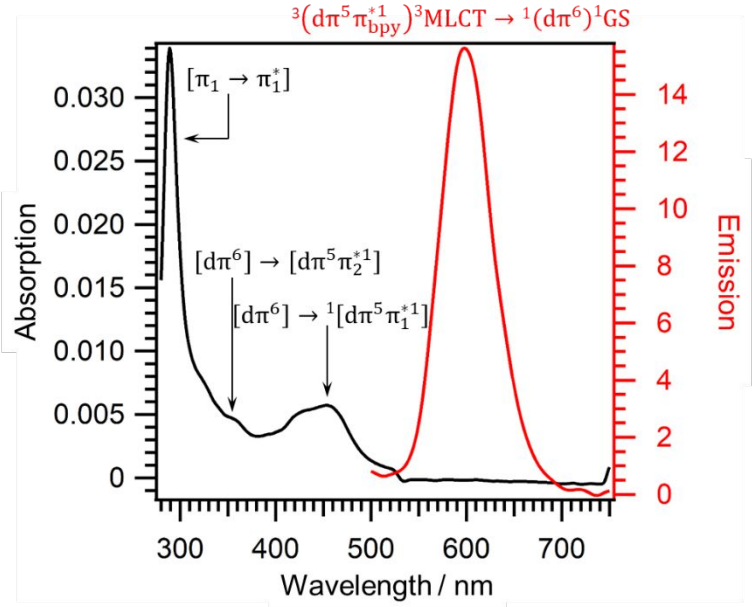

Figure S3. Adsorption (black) and emission (red) spectra for the **Ru-IgG** conjugate with labels corresponding to the main transitions and their respective electronic configurations (MLCT: metal-to-ligand charge transfer; GS: ground state). Spectra acquired by FP-6500 (Jasco, Tokyo, Japan). Excitation wavelength was 450 nm.

3.3 Beads labelling with Ru-IgG-biotin conjugate (Ru@bead)

The streptavidin-coated magnetic beads in the amount of 1 µL were washed three times with 0.2 M PB (pH 7), 50 µL of the **Ru-IgG-biotin** solution were added, and the mixture was incubated at 25 °C for 30 min. After incubation, the magnetic beads were washed first with 0.05 wt% Tween 20 in PB twice, then with PB three times, finally 5 µL of 100 mM TPrA in PB were added. This solution is used for one single ECL measurement.

3.4 Ruthenium complex remaining confirmation after washing procedure

To evaluate if unbound **Ru-IgG-biotin** is completely removed after the beads labelling procedure,

the ECL of supernatant was investigated. The ECL profiles obtained from the supernatants are shown in Figure S4. After five cycles of washing (0.05 wt% Tween 20 in PB twice and PB three times), the ECL emission was not observed except after the first one. This confirm that unbound **Ru-IgG-biotin** conjugate was completely removed from the beads suspension and does not enter the electrochemical cell which might lead to uncorrected observations and interpretations of the ECL results.

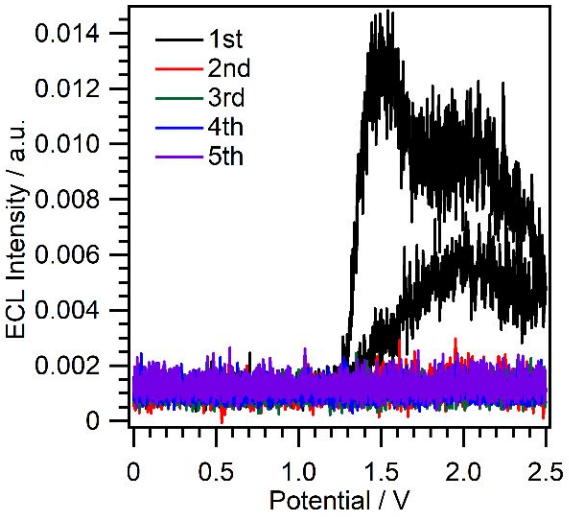

Figure S4. ECL intensity for the solutions used for washing the beads conjugate (supernatant) with the addition of 100 mM TPrA in 0.2 M PB (pH 7): 1st washing solution (black), 2nd (red), 3rd (green), 4th (blue) and 5th (violet).

4. Thermodynamics of Tris(2,2'-bipyridine)ruthenium(II)/TPrA system

Table S1. Selected redox couples and potentials. P_1 refers to the degradation of $TPrA^{\bullet}$ by oxidation and following hydrolysis.[3]

	$Ru(bpy)_3^{3+}/Ru(bpy)_3^{2+}$	$Ru(bpy)_3^{2+}/Ru(bpy)_3^{+}$	$TPrA/TPrA^{\bullet+}$	$TPrA^{\bullet}/P_1$
E^0 / V (vs NHE)	1.27[4]	−1.23[4]	1.12[5]	−1.46[6]

The energetic parameters of the reactions involved in the ECL (Scheme 1 and 2 of main text) were calculated as follow based on the Rehm-Weller equation:[7,8,9,10]

$$\Delta G = \left(E^0_{Ox} - E^0_{Red}\right) - E_{00} - \frac{e^2}{4\pi\varepsilon_0\varepsilon r} \qquad \text{(S1)}$$

E^0_{Ox} is the standard potentials of the donor

E^0_{Red} is the standard potentials of the acceptor

E_{00} is the energy of the excited state

$\frac{e^2}{4\pi\varepsilon_0\varepsilon r}$ is the Coulombic term to account for the electrostatic attraction at an encounter distance r in a

solvent having a dielectric constant ε (ε_0 is the dielectric constant of vacuum). To simplify, it is possible to be omitted because the energy involved is substantially lower than that involved in the electron transfer reaction.

5. ECL spectra

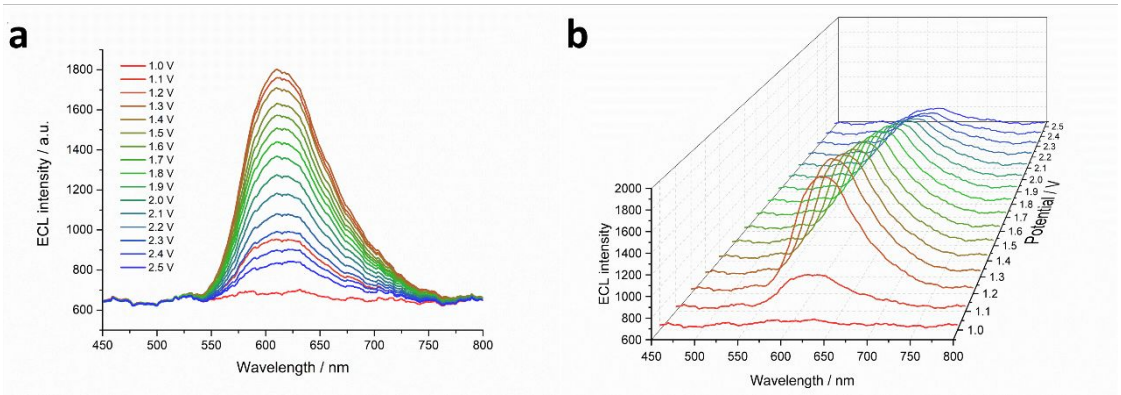

Figure S5. ECL spectra (a) and a 3D plot (b) for 40 μM $Ru(bpy)_3^{2+}$ and 100 mM TPrA in 0.2 M PB (pH 8.0) during the forward scan of cyclic voltammetry. Scan rate: 100 mV s^{-1}. Time integration of each spectrum: 1 s.

6. Electrochemical impedance spectrometry (EIS) measurements

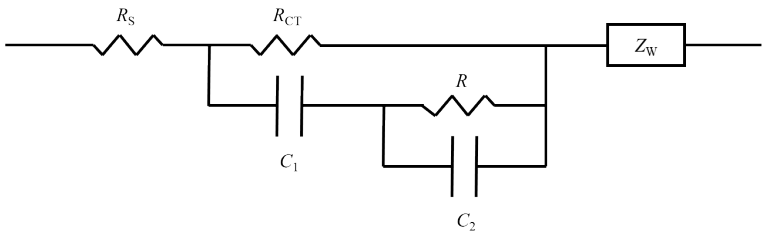

Figure S6. Equivalent circuit model utilized for the fitting the EIS measurements. R_S is solution resistance, R_{CT} is the charge transfer resistance of TPrA, C_1 is the double layer capacitance, R and C_2 is the resistance and the capacitance, respectively, given by the surface modification of BDD in PB only, and Z_W is Warburg impedance.

The apparent electron transfer constant for TPrA oxidation (k_{ET}) was calculated from eq. S1-S7, as we showed previously.[2] The resistance for charge transfer (R_{CT}) can be expressed as eq. S1, where R is the gas constant is temperature is T, the number of electrons involved in the reaction is n and Faraday constant is F. The exchange current density, i_0, is given by eq. S2, where C represents the concentration of the reactant, TPrA in this case. Therefore, eq. S1 and eq. S2 can be rearranged into eq. S3. In addition, TPrA is in equilibrium with its protonated form i.e., $TPrAH^+$ (eq. S4), and the concentration

of unprotonated TPrA is calculated from eq. S5, where K_a is the equilibrium constant ($pK_{a\,TPrA} = 10.4$)[5] and $[TPrA]_{tot}$ denotes the total concentration (TPrA and $TPrAH^+$). Finally, k_{ET} can be calculated from eq. S6 from a single TPrA concentration.

$$R_{ct} = \frac{RT}{nFi_0} \quad \text{(S2)}$$

$$i_0 = nFAk^0C \quad \text{(S3)}$$

$$\frac{1}{R_{ct}} = \frac{F^2Ak^0}{RT}[TPrA] \quad \text{(S4)}$$

$$TPrAH^+ \rightleftarrows TPrA + H^+ \quad \text{(S5)}$$

$$[TPrA] = \frac{K_a}{[H^+] + K_a}[TPrA]_{tot} \quad \text{(S6)}$$

$$k^0 = \frac{RT}{R_{ct}F^2A} \times \frac{[H^+] + K_a}{K_a[TPrA]_{tot}} \quad \text{(S7)}$$

However, we used four TPrA concentrations to attain a more reliable value for the k_{ET}, expressed as eq. S7.

$$k_{ET} = \frac{RT}{F^2A} \times \text{slope} \quad \text{(S8)}$$

The Nyquist plots by EIS measurements and linear approximations for the electron transfer resistance are shown in Figure S7 and S8. The gradient of the approximate line is equivalent to the electron transfer constant at each potential.

The relationship of k_{ET} with potentials can be expressed as:[11,12]

$$k_{ET} = k^0_{ET}\exp\left[(1-\alpha)\frac{nF}{RT}(E - E^0)\right] \quad \text{(S9)}$$

k^0_{ET} is the standard rate constant of electron transfer at standard potential E^0

α is the transfer coefficient

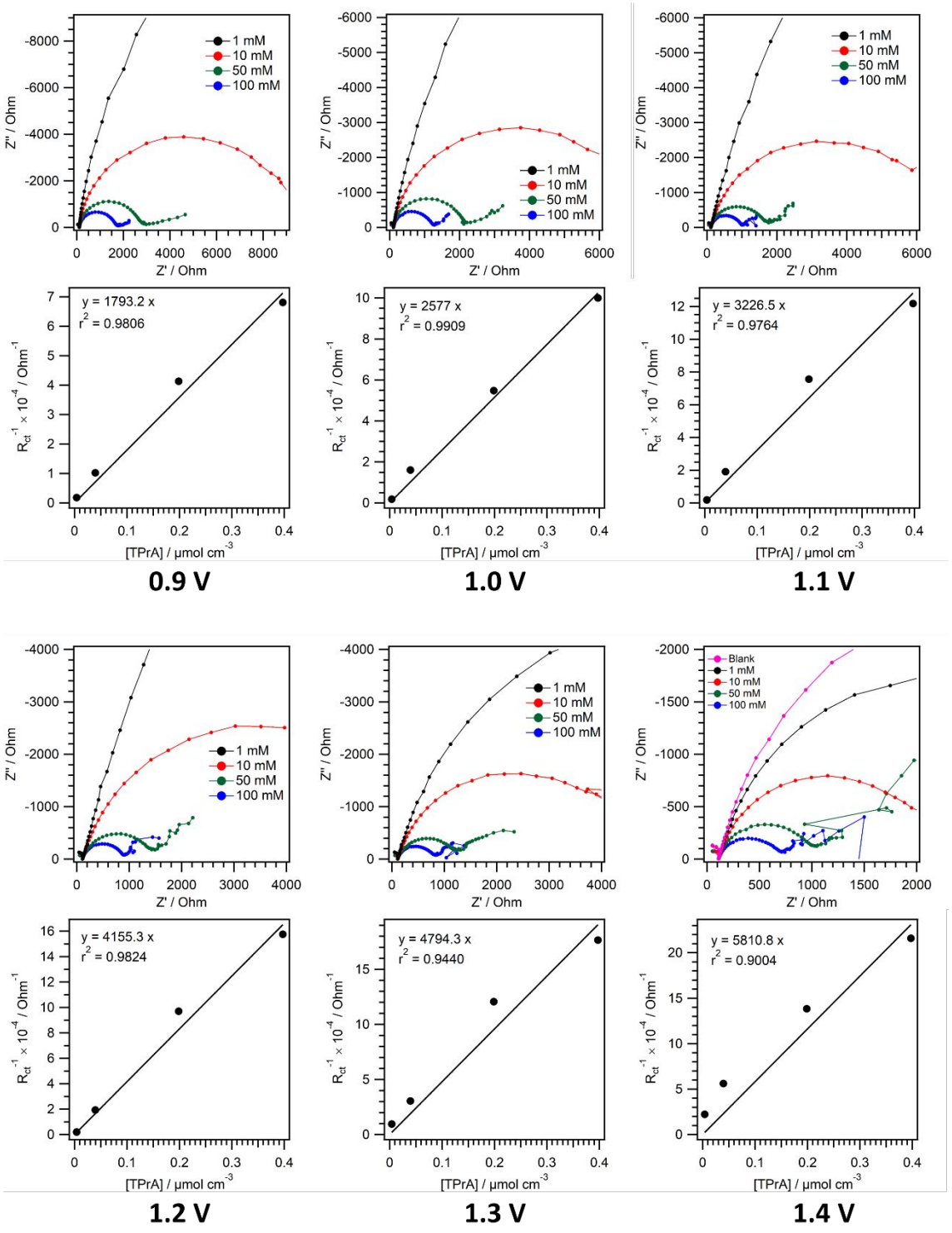

Figure S7. Nyquist plot and R_{CT}^{-1} as a function of the free TPrA concentration (for 1, 10, 50 and 100 mM total TPrA) in 0.2 M PB (pH 8.0) on CR-BDD. Potential applied as indicated, from 0.9 V to 1.4 V, as indicated. Frequency range: 1 MHz – 10 mHz.

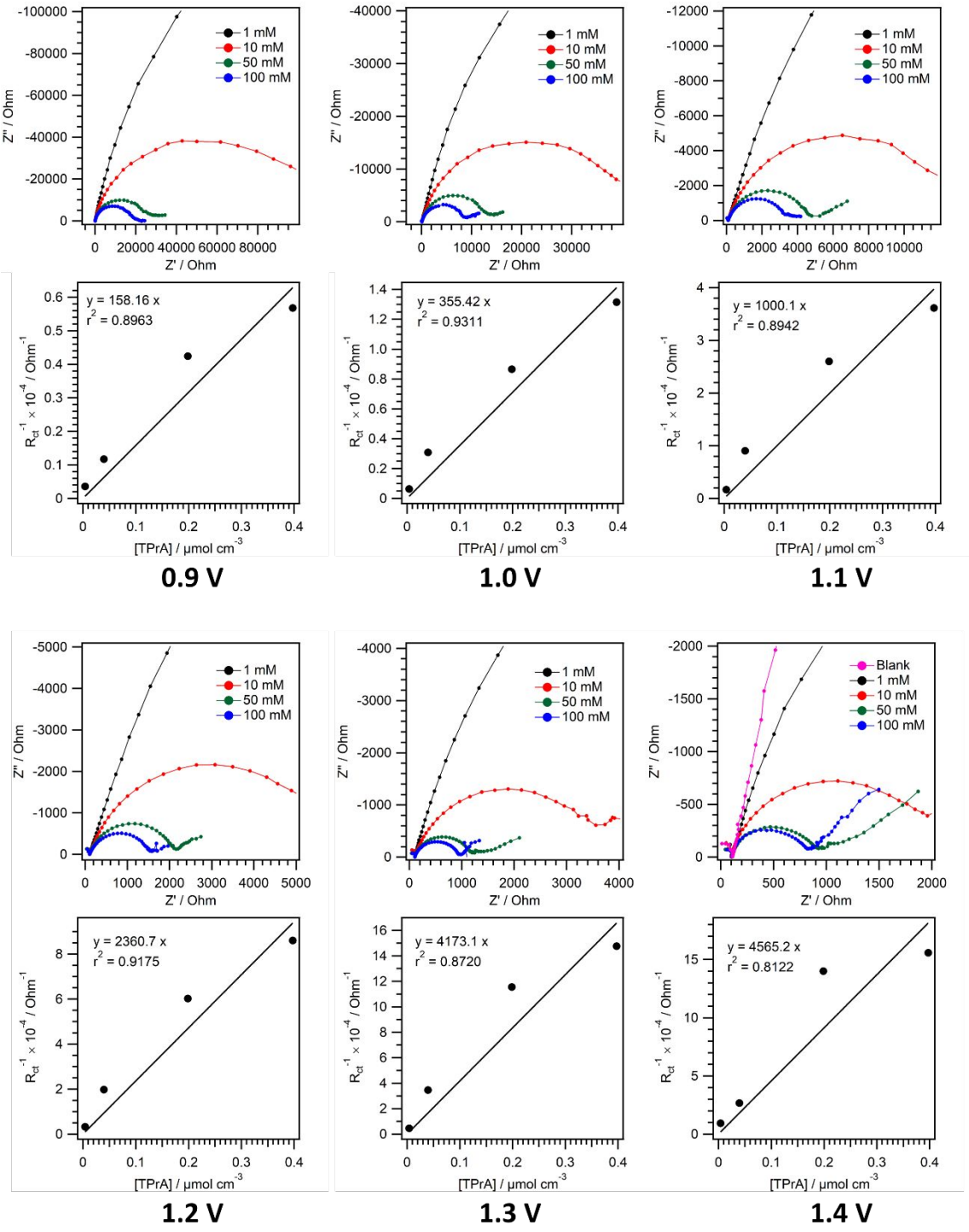

Figure S8. Nyquist plot and R_{CT}^{-1} as a function of the free TPrA concentration (for 1, 10, 50 and 100 mM total TPrA) in 0.2 M PB (pH 8.0) on AO-BDD. Potential applied as indicated, from 0.9 V to 1.4 V. Frequency range: 1 MHz – 10 mHz.

7. Optimization of measurement conditions

7.1 TPrA concentration

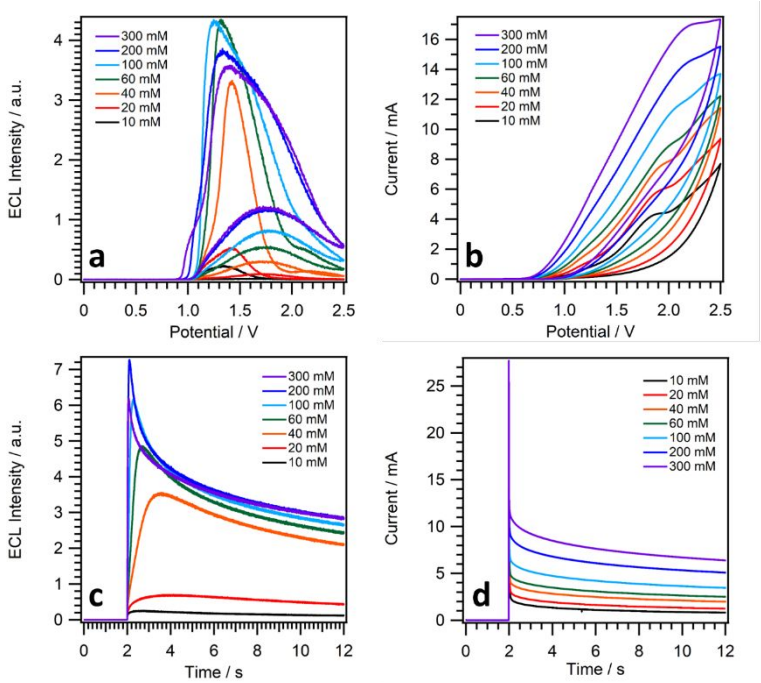

Figure S9. ECL intensity (a) and cyclic voltammogram (b); scan rate 100 mV s^{-1}. ECL intensity (c) (used for Figure 3 of the main text) and current (d) by chronoamperometry (E_1 = 0 V, t_1 = 2 s; E_2 = 1.4 V, t_2 = 10 s). Solution: 10 µM $Ru(bpy)_3^{2+}$ and 1, 10, 20, 40, 60, 100, 200 and 300 mM TPrA in 0.2 M PB (pH 8.0) on CR-BDD.

7.2 pH of the solutions

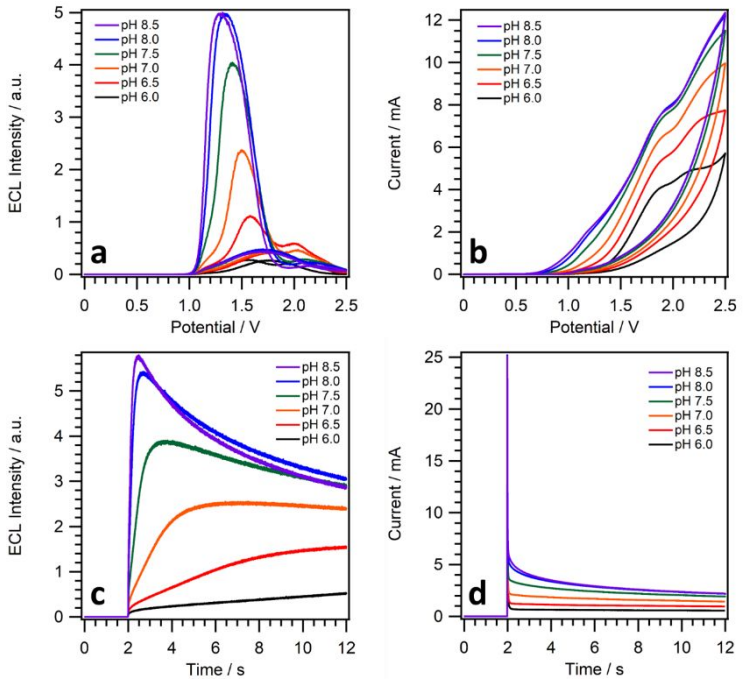

Figure S10. ECL intensity (a) and cyclic voltammogram (b); scan rate 100 mV s^{-1}. ECL intensity (c) (used for Figure 3 of the main text) and current (d) by chronoamperometry (E_1 = 0 V, t_1 = 2 s; E_2 = 1.4 V, t_2 = 10 s). Solution: 10 µM $Ru(bpy)_3^{2+}$ and 40 mM TPrA in 0.2 M PB (pH 6.0, 6.5, 7.0, 7.5, 8.0 and 8.5) on CR-BDD.

8. Stability of ECL signal

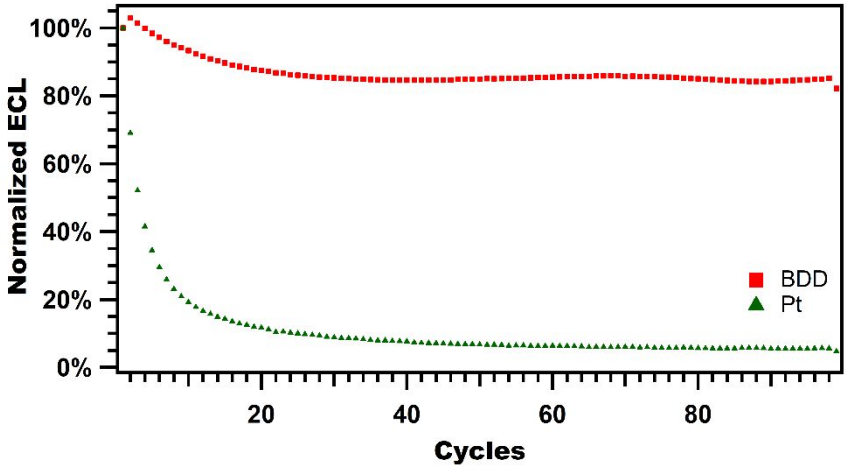

Figure S11. ECL signal by continuous chronoamperometry (E_1 = 0 V, t_1 = 3 s; E_2 = 1.4 V, t_2 = 0.5 s). Number of repetitions: 100 cycles. Solution: 10 µM $Ru(bpy)_3^{2+}$ and 100 mM TPrA in 0.2 M PB (pH 8.0). The BDD retains an 84.3% of the ECL signal, while Pt 4.6%, after 100 cycles.

9. Surfactant effect

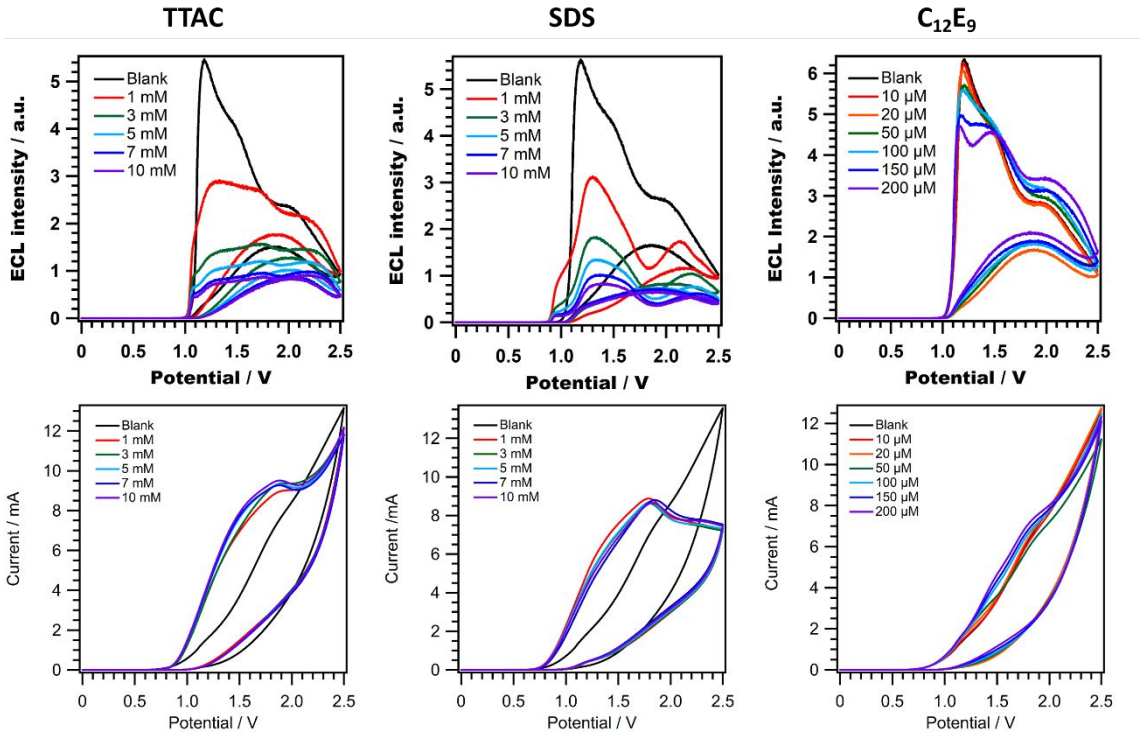

Figure S12. ECL intensity and cyclic voltammograms for surfactants (TTAC, SDS, and $C_{12}E_9$) at different concentrations with 10 µM $Ru(bpy)_3^{2+}$ and 100 mM TPrA in 0.2 M PB (pH 8.0) on CR-BDD. Scan rate: 100 mV s^{-1}.

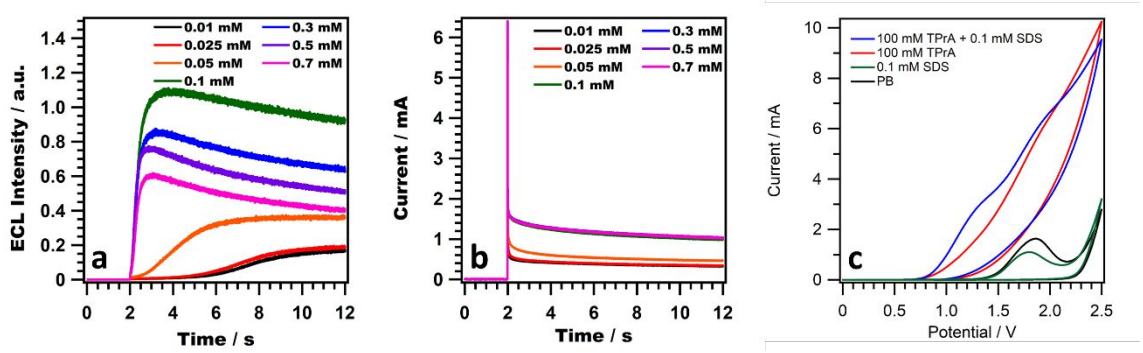

Figure S13. ECL intensity (a) and current (b) by chronoamperometry (E_1=0 V, t_1 = 2 s; E_2 = 0.95 V, t_2 = 10 s) for 10 µM $Ru(bpy)_3^{2+}$ and 100 mM TPrA in 0.2 M PB (pH 8.0) on CR-BDD with various additions of SDS. Cyclic voltammetry (c) of 0.2 M PB (black), 0.1 mM SDS in 0.2 M PB (green), 100 mM TPrA in 0.2 M PB (red), and 0.1 mM SDS with 100 mM TPrA in 0.2 M PB (blue), all solution at pH 8.

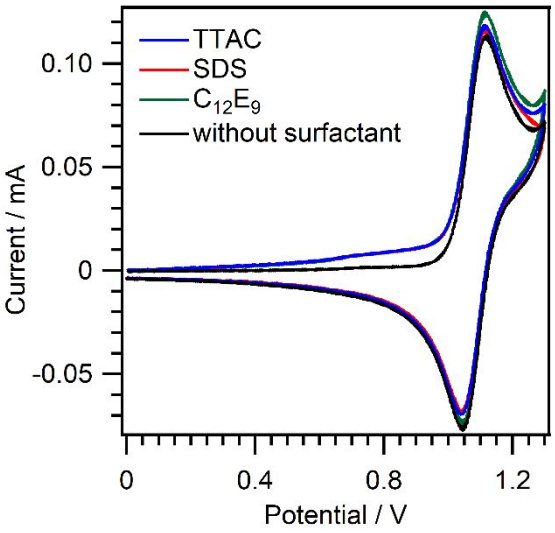

Figure S14. Cyclic voltammetry of 1mM $Ru(bpy)_3^{2+}$ in 0.2 M PB (pH 8.0) at CR-BDD with 10 mM TTAC, 0.1 mM SDS, and 200 μM $C_{12}E_9$. $E_{1/2}$ = 1.08 vs Ag/AgCl (KCl sat).

10. Halide ion effect

The results of halide ions effect were reported in Figure S14. Note that all the solutions contain 20μM Cl^- because $Ru(bpy)_3Cl_2$ was used to make the solutions. Chloride ions had little effect on the ECL intensity and current (Figure S14a and b). Bromide ions decreased the ECL intensity around 2.0 V with their concentration increasing (Figure S14c), and in term of the current, it was clear the oxidation process upon bromide (Figure S14d). Iodide ions quenched significantly the ECL intensity from the small concentration added (Figure S14e), while the oxidation current of iodine is observed clearly only for the higher concentrations (Figure S14f).

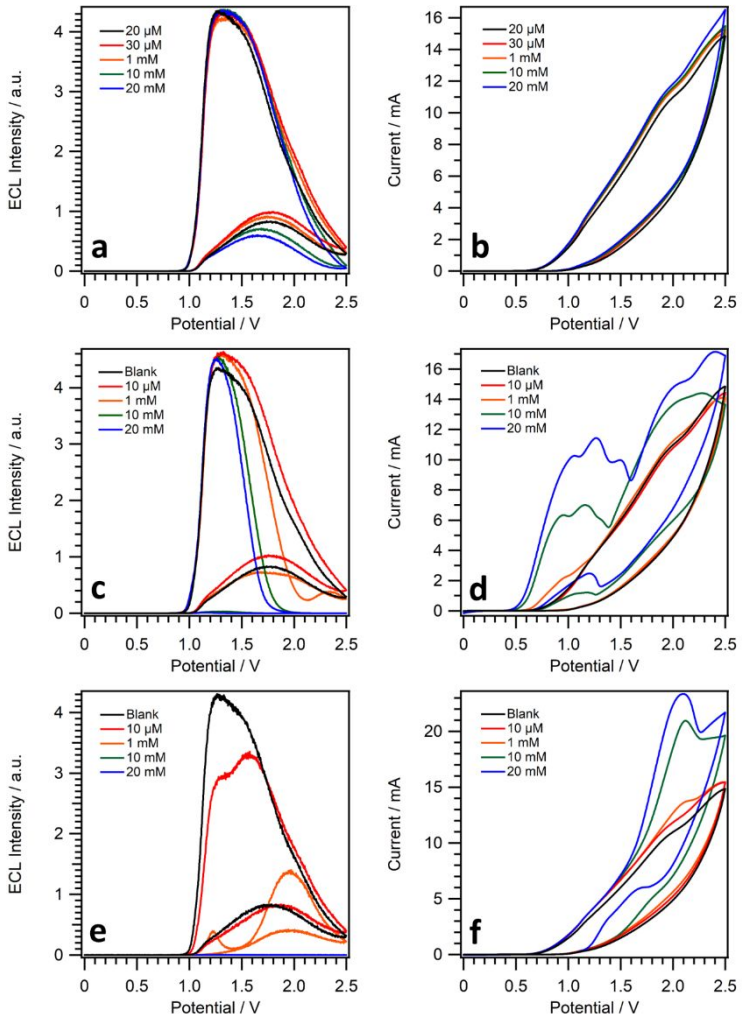

Figure S15. ECL intensity (a) and cyclic voltammogram (b) for 10 µM $Ru(bpy)_3^{2+}$ and 100 mM TPrA with 20 µM, 30 µM, 1 mM, 10 mM and 20 mM Cl^- in 0.2 M PB (pH 8.0) on CR-BDD. ECL intensity (c) and cyclic voltammogram (d) for 10 µM $Ru(bpy)_3^{2+}$ and 100 mM TPrA with 0 µM, 10 µM, 1 mM, 10 mM and 20 mM Br^- in 0.2 M PB (pH 8.0) on CR-BDD. ECL intensity (e) and cyclic voltammogram (f) for 10 µM $Ru(bpy)_3^{2+}$ and 100 mM TPrA with 0 µM, 10 µM, 1 mM, 10 mM and 20 mM I^- in 0.2 M PB (pH 8.0) on CR-BDD.

11. ECL immunoassay

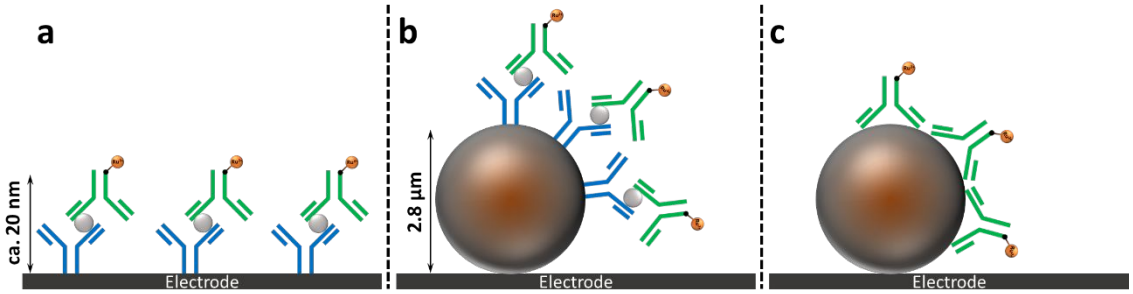

Figure S16. Schematic representation of ECL immunoassay: (a) directly bound onto the electrode surface and (b) bound on magnetic microbeads. The approach used in this work (**Ru@bead**) to mimic the ECL immunoassay by microbeads (c). Primary antibody (blue), antigen (gray), secondary antibody (green), and ruthenium ECL label (orange).

12. ECL imaging

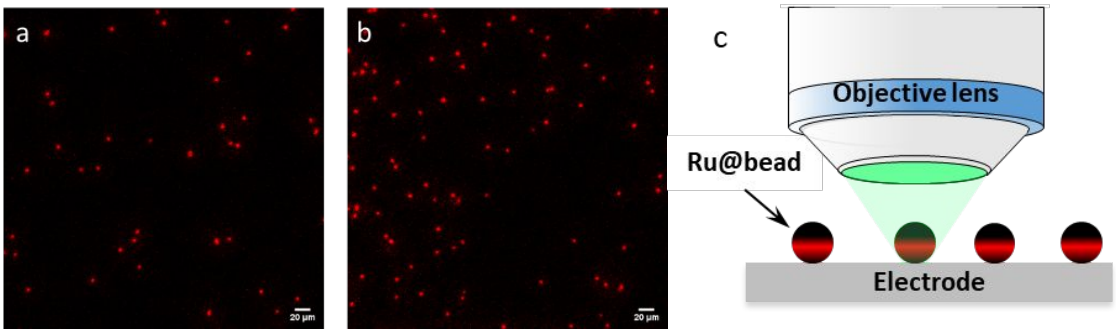

Figure S17. ECL images for **Ru@bead** on AO-BDD (a) and CR-BDD (b). Electrochemical measurements were performed by chronoamperometry applying 1.7 V as emission potential for 4 s, with a magnification of 20x and an integration time of 8 s. Scale bar: 20 µm. Scheme of ECL imaging (c); detailed information on ECL microscopy setup is available from previous publications.[13,14,15]

13. Optimization of measurement conditions with the Ru@bead

13.1. Pretreatment

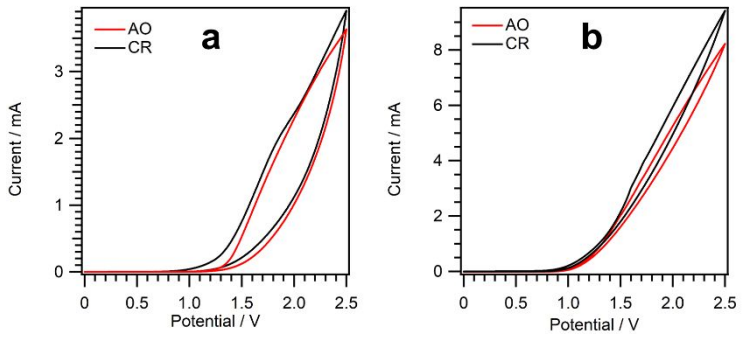

Figure S18. Cyclic voltammetry for **Ru@bead** with 100 mM TPrA in 0.2 M PB (pH 7.0) on CR-BDD (black) and AO-BDD (red). Multibeads detection by PMT (a) and single bead by ECL imaging (b). Scan rate: 100 mV s^{-1}.

13.2. SDS concentration

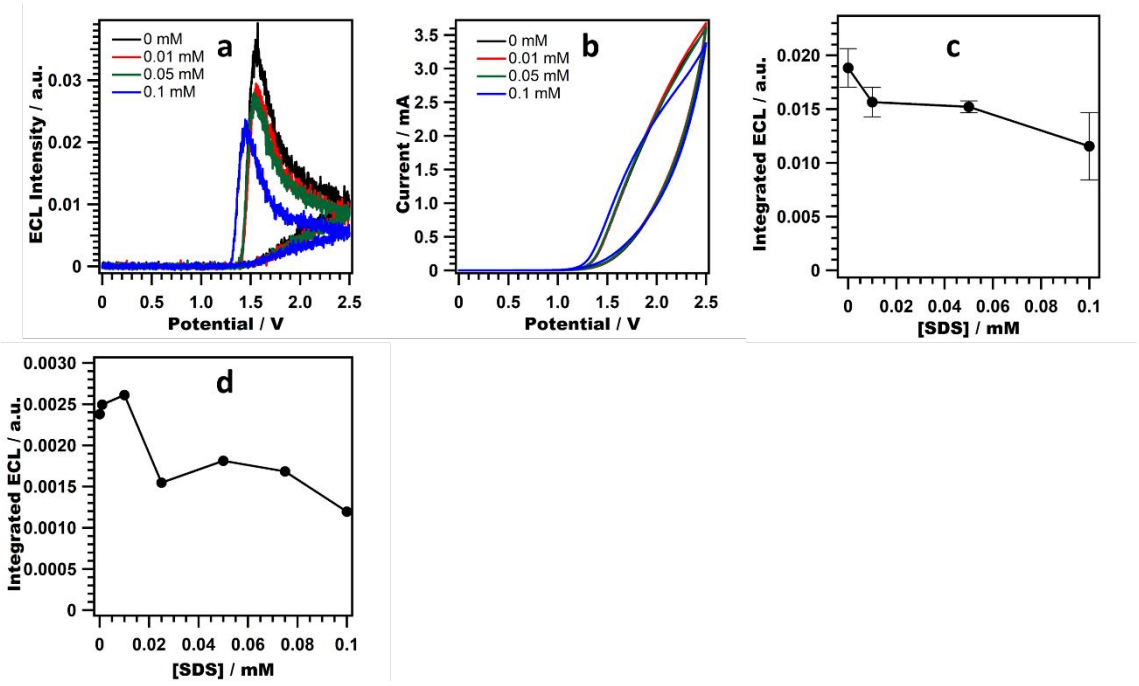

Figure S19. ECL intensity (a) and cyclic voltammograms (b) for Ru@bead with 100 mM TPrA in 0.2 M PB (pH 7.0) on AO-BDD (black), and addition of 0.01 (red), 0.05 (green), and 0.1 (blue) mM SDS. Scan rate: 100 mV s^{-1}. Integrated ECL for Ru@bead on AO-BDD (c) as function of SDS concentration. Integrated ECL for Ru@bead on CR-BDD (d) as function of SDS concentration with 100 mM TPrA in 0.2 M PB (pH 8.0).

13.3. pH

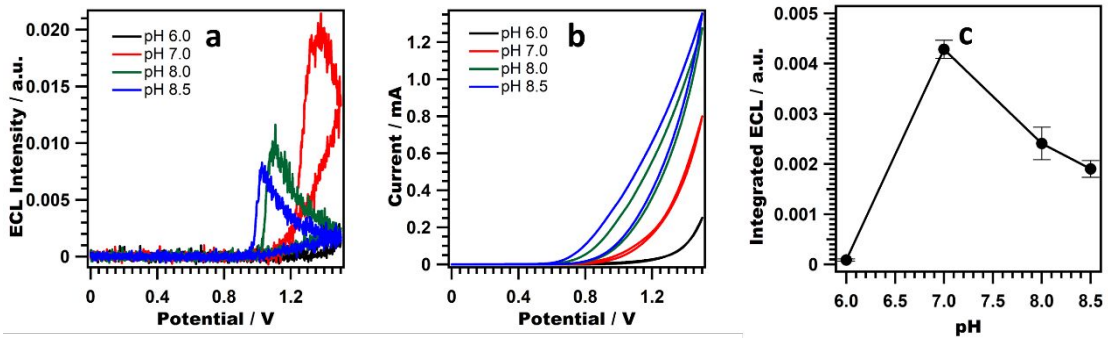

Figure S20. ECL intensity (a) and cyclic voltammograms (b) for Ru@bead with 100 mM TPrA in 0.2 M PB on AO-BDD at pH 6.0 (black), 7.0 (red), 7.5 (green), and 8.0 (blue). Scan rate: 100 mV s^{-1}. Integrated ECL as function of pH (c).

13.4. TPrA concentration

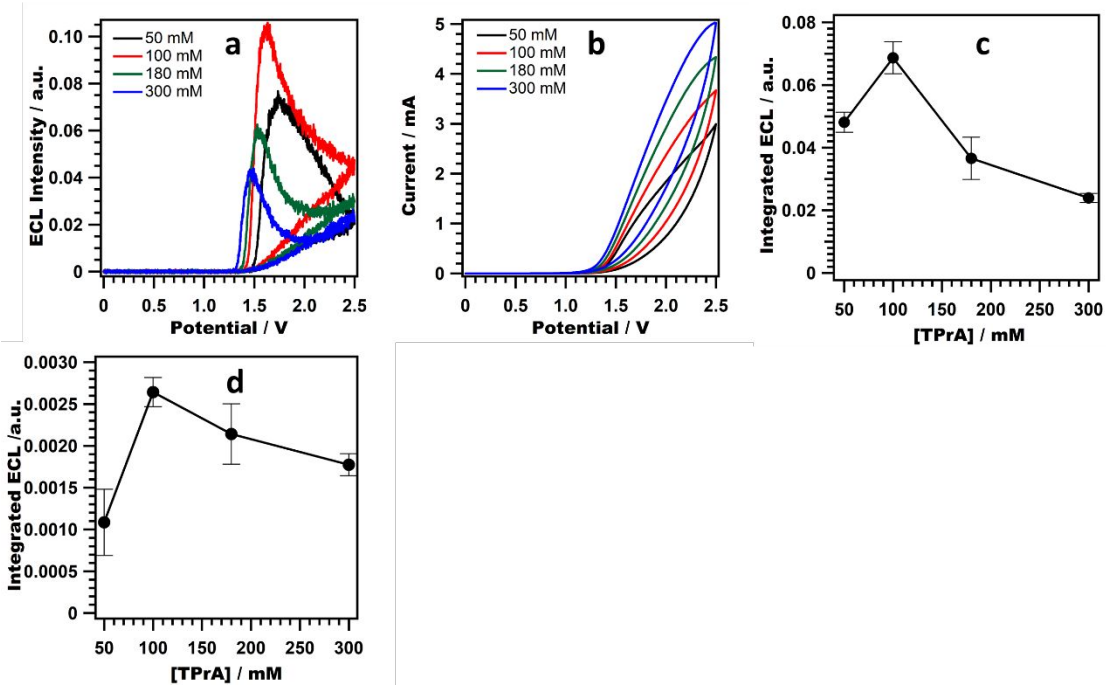

Figure S21. ECL intensity (a), cyclic voltammograms at 100 mV s^{-1} (b) and integrated ECL (c) for Ru@bead with 50 (black), 100 (red), 180 (green), 300 (blue) mM TPrA in 0.2 M PB (pH 7.0) on AO-BDD. Integrated ECL for Ru@bead as function of TPrA concentration in 0 .2 M PB (pH 8.0) on CR-BDD (d).

13.5. Applied potential for BDD

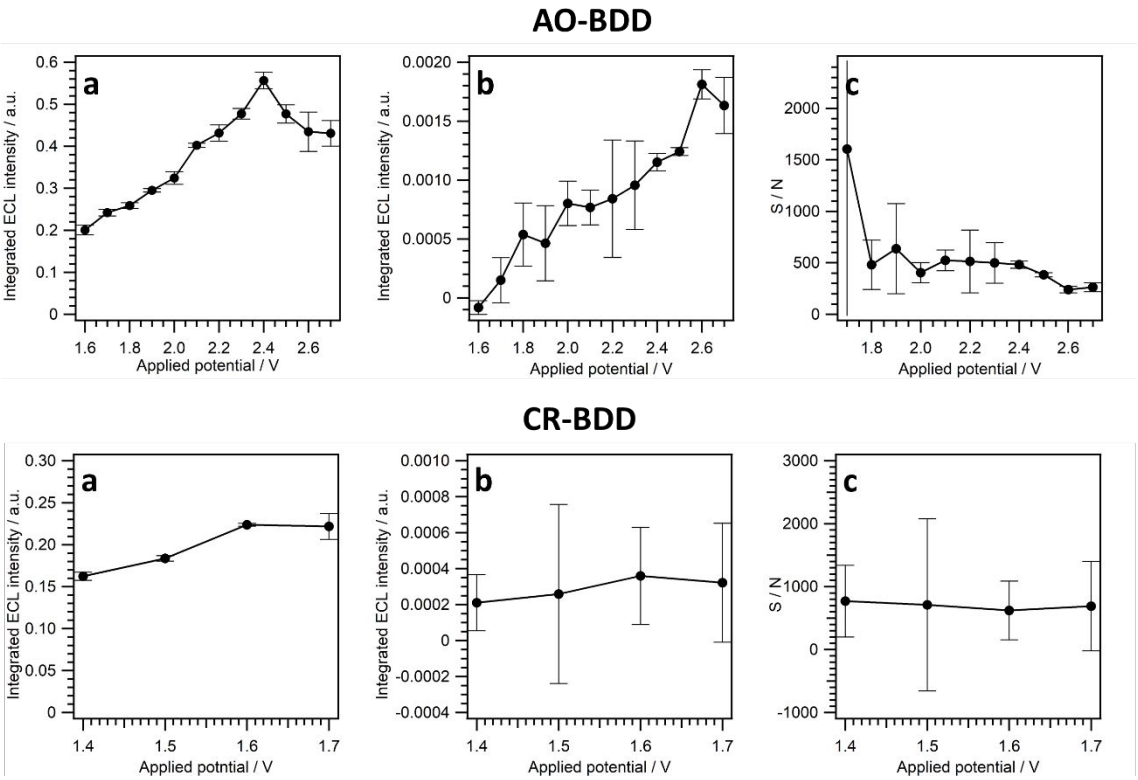

Figure S22. Integrated ECL intensity by chronoamperometry (E_1 = 0 V; t_1 = 2 s; E_2 = E_x V; t_2 = 10 s) as a function of the applied potential (E_x) for Ru@bead (a), background without Ru@bead (b) and Signal-to-Noise ratio (c) for AO-BDD and CR-BDD electrodes. Solution: 100 mM TPrA in 0.2 M PB (pH 7.0). Error bar shows the standard deviation (N = 3).

12.6. Applied potential for BDD

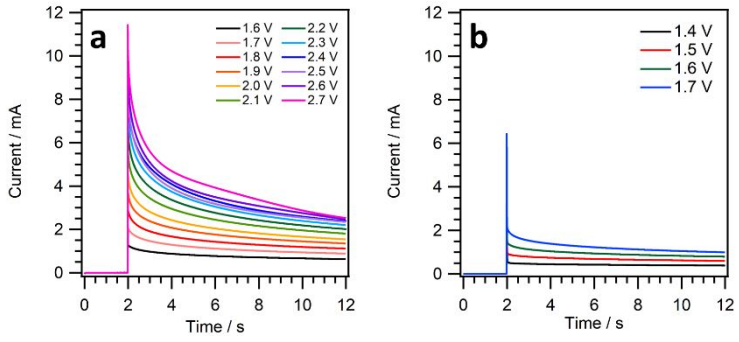

Figure S23. Chronoamperometry data of Figure S22, (E_1 = 0 V; t_1 = 2 s; E_2 = E_x V; t_2 = 10 s) as a function of the applied potential (E_x) for Ru@bead for AO-BDD (a) and CR-BDD (b). Solution: 100 mM TPrA in 0.2 M PB (pH 7.0).

13.7. Applied potential for Pt

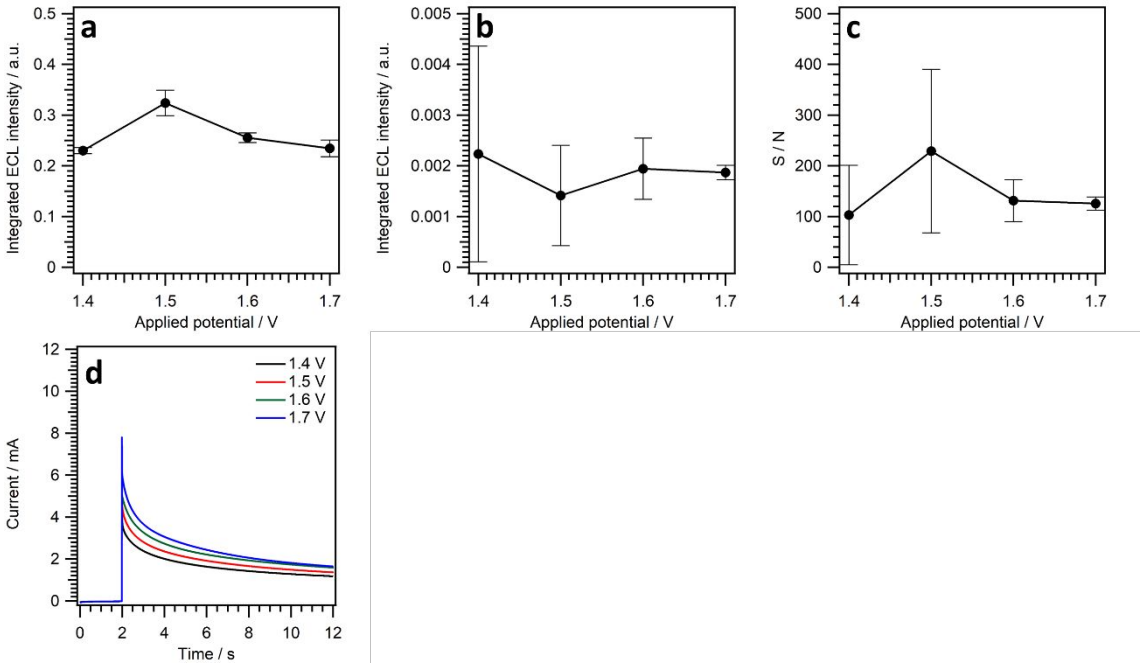

Figure S24. Integrated ECL intensity by chronoamperometry (E_1 = 0 V; t_1 = 2 s; E_2 = E_x V; t_2 = 10 s) as a function of the applied potential (E_x) for Ru@bead (a), background without Ru@bead (b), Signal-to-Noise ratio (c) and chronoamperometry data of Figure S24a (d) for Pt electrode. Solution: 0.1wt% $C_{12}E_9$ and 180 mM TPrA in 0.2 M PB (pH 6.9). Error bar shows the standard deviation (N = 3).

14. AO-BDD, CR-BDD and Pt comparison with Ru@Bead

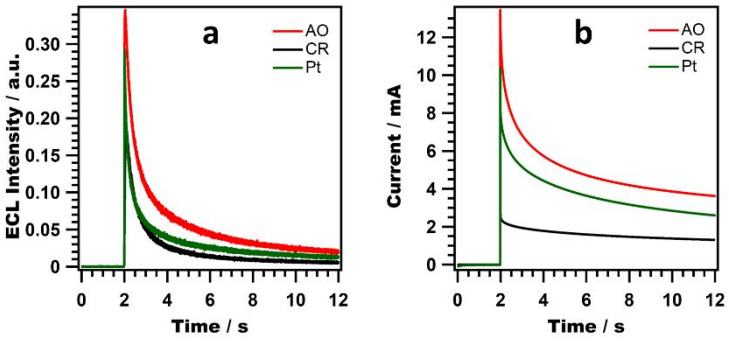

Figure S25. ECL intensity (a) and current (b) of **Ru@bead** for AO-BDD (red), CR-BDD (black) and Pt (green) by two steps chronoamperometry (E_1 = 0 V; t_1 = 2 s; E_2 = E_x V; t_2 = 10 s) where E_x is 2.4 V for AO-BDD, 1.6 V for CR-BDD, and 1.5 V for Pt electrodes. Solutions: **Ru@bead** with 100 mM TPrA in 0.2 M PB (pH 7.0) for both AO-BDD and CR-BDD electrodes; **Ru@bead** with 180 mM TPrA and 0.1wt% $C_{12}E_9$ in 0.2 M PB (pH 6.9) for Pt electrode.

15. BDD and GC comparison with Ru@Bead

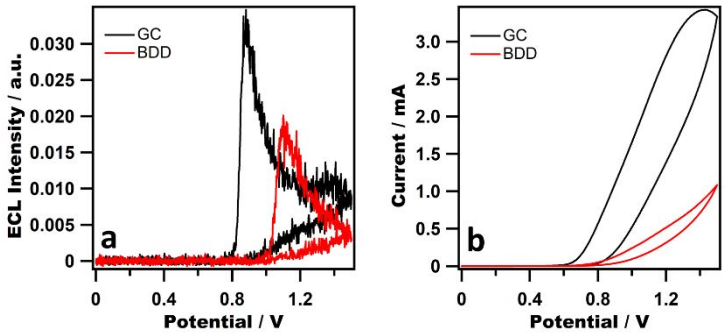

Figure S26. ECL intensity (a) and cyclic voltammogram (b) of **Ru@bead** for BDD (red) and GC (black) by CV. Scan rate: 100 mV s^{-1}. Solution: **Ru@bead** with 100 mM TPrA in 0.2 M PB (pH 8.0).

16. References

(1) Xu, J.; Yokota, Y.; Wong, R.A.; Kim, Y.; Einaga, Y. Unusual Electrochemical Properties of Low-Doped Boron-Doped Diamond Electrodes Containing sp^2 Carbon. *J. Am. Chem. Soc.* **2020**, *142* (5), 2310-2316.

(2) Sakanoue, K.; Fiorani, A.; Irkham; Einaga, Y. Effect of Boron-Doping Level and Surface Termination in Diamond on Electrogenerated Chemiluminescence. ACS Appl. Electron. Mater. 2021, 3 (9), 4180-4188.

(3) Miao, W.; Choi, J.-P.; Bard, A. J. Electrogenerated Chemiluminescence 69: The Tris(2,2'-bipyridine)ruthenium(II),($Ru(bpy)_3^{2+}$)/Tri-*n*-propylamine (TPrA) System Revisited−A New Route Involving $TPrA^{\bullet+}$ Cation Radicals. J. *Am. Chem. Soc.* **2002**, *124* (48), 14478-14485.

(4) Thompson, D. W.; Ito, A.; Meyer, T. J. $[Ru(bpy)_3]^{2+*}$ and Other Remarkable Metal-to-Ligand Charge Transfer (MLCT) Excited States. *Pure Appl. Chem.* **2013**, (7), 1257-1305.

(5) Kanoufi, F.; Zu, Y.; Bard, A. J. Homogeneous Oxidation of Trialkylamines by Metal Complexes and Its Impact on Electrogenerated Chemiluminescence in the Trialkylamine/$Ru(bpy)_3^{2+}$ System. *J. Phys. Chem. B* **2001**, *105* (1), 210-216.

(6)Lai, R. Y.; Bard, A. J. Electrogenerated Chemiluminescence. 70. The Application of ECL to Determine Electrode Potentials of Tri-*n*-propylamine, Its Radical Cation, and Intermediate Free Radical in MeCN/Benzene Solutions. *J. Phys. Chem. A* **2003**, *107* (18), 3335-3340.

(7) Rehm, D.; Weller, A. Kinetics of Fluorescence Quenching by Electron and H-Atom Transfer. *Isr. J. Chem.* **1970**, *8* (2), 259-271.

(8) Farid, S.; Dinnocenzo, J. P.; Merkel, P. B.; Young, R. H.; Shukla, D.; Guirado, G. Reexamination of the Rehm-Weller Data Set Reveals Electron Transfer Quenching That Follows a Sandros-Boltzmann Dependence on Free Energy. *J. Am. Chem. Soc.* **2011**, *133* (30), 11580-11587.

(9) Rosspeintner, A.; Angulo, G.; Vauthey, E. Bimolecular Photoinduced Electron Transfer Beyond the

Diffusion Limit: The Rehm-Weller Experiment Revisited with Femtosecond Time Resolution. *J. Am. Chem. Soc.* **2014**, *136* (5), 2026-2032.

(10) Kerr, E.; Doeven, E. H.; Wilson, D. J. D.; Hogan, C. F.; Francis, P. S. Considering the chemical energy requirements of the tri-*n*-propylamine co-reactant pathways for the judicious design of new electrogenerated chemiluminescence detection systems. *Analyst* **2016**, *141* (1), 62-69.

(11) Bard, A. J.; Faulkner, L. R. *Electrochemical Methods: Fundamentals and Applications, 2nd ed.*; John Wiley & Sons: NewYork, **2001**, pp. 94-97.

(12) Oldham, K. B. The potential-dependence of electrochemical rate constants. *J. Electroanal. Chem.* **1968**, *16* (2), 125-130.

(13) Zanut, A.; Fiorani, A.; Canola, S.; Saito, T.; Ziebart, N.; Rapino, S.; Rebeccani, S.; Barbon, A.; Irie, T.; Josel, H.-P.; Negri, F.; Marcaccio, M.; Windfuhr, M.; Imai, K.; Valenti, G.; Paolucci, F. Insights into the mechanism of coreactant electrochemiluminescence facilitating enhanced bioanalytical performance. *Nat. Commun.* **2020**, *11*, 2668.

(14) Zanut, Z.; Palomba, F.; Rossi Scota, M.; Rebeccani, S.; Marcaccio, M.; Genovese, D.; Rampazzo, E.; Valenti, G.; Paolucci, F.; Prodi, L. Dye-Doped Silica Nanoparticles for Enhanced ECL-Based Immunoassay Analytical Performance. *Angew. Chem. Int. Ed.* **2020**, *59* (49), 21858-21863.

(15) Fiorani, A.; Han, D.; Jiang, D.; Fang, D.; Paolucci, F.; Sojic, N.; Valenti, G. Spatially resolved electrochemiluminescence through a chemical lens. *Chem. Sci.* **2020**, *11* (38), 10496-10500.